Geochemistry Geophysics Geosystems G3

Article
Volume 12, Number 7
19 July 2011
Q0AD15, doi:10.1029/2010GC003365
ISSN: 1525-2027

Published by AGU and the Geochemical Society

Structural styles across the Nankai accretionary prism revealed from LWD borehole images and their correlation with seismic profile and core data: Results from NanTroSEIZE Stage 1 expeditions

Yasuhiro Yamada
Department of Earth Resources Engineering, Kyoto University, Kyoto 615-8540, Japan (yamada@earth.kumst.kyoto-u.ac.jp)

Lisa McNeill
School of Ocean and Earth Science, National Oceanography Centre, Southampton, University of Southampton, Southampton SO14 3ZH, UK (lcmn@noc.soton.ac.uk)

J. Casey Moore
Earth and Planetary Sciences Department, University of California, Santa Cruz, California 95064, USA (cmoore@pmc.ucsc.edu)

Yasuyuki Nakamura
Atmosphere and Ocean Research Institute, University of Tokyo, Kashiwa, Chiba 277-8568, Japan (saru@aori.u-tokyo.ac.jp)

[1] Four drill sites of IODP NanTroSEIZE Stage 1 Expedition transected the Nankai Trough, offshore SW Japan, from the deformation front to the Kumano fore-arc basin. Borehole resistivity images from the logging-while-drilling (LWD) data were analyzed to extract orientations of faults, fractures, and bedding planes to examine the structural styles. On the basis of these features, drilling intervals were classified into fore-arc basin deposits, surface slope sediments, and deformed accretionary wedge, and these can be compared with characteristics from seismic profiles and core structural data. Bedding orientations identified in these three data sets are generally comparable, but the difference in resolution between the data sets produces different results in interpretation where geology is highly deformed or includes finer internal structures. Faults can also be correlated between these three data sets, but the differences in their appearance require special attention for accurate correlation. Many faults imaged in seismic profiles actually consist of microfracture systems, as shown in cores, that can also be identified in borehole images. Some clear faults in seismic profiles cannot be identified in borehole images, probably because of their minimal resistivity contrast with the surrounding rocks or a more complex fault zone at the borehole scale. These results suggest that these three data sets can be used to extract not only the general structure but also different styles of deformation at different scales from core samples (mm to cm), to LWD (mm to 10 m), to seismic (10 m to tens of km). This correlation requires a deep understanding of the resolution and shortcomings of each methodology.

Components: 9800 words, 15 figures.

Keywords: LWD; accretionary prism; borehole images; faults; folds; seismic.

Index Terms: 8005 Structural Geology: Folds and folding; 8010 Structural Geology: Fractures and faults; 8170 Tectonophysics: Subduction zone processes (1031, 3060, 3613, 8413).

Received 6 October 2010; **Revised** 17 May 2011; **Accepted** 25 May 2011; **Published** 19 July 2011.

Yamada, Y., L. McNeill, J. C. Moore, and Y. Nakamura (2011), Structural styles across the Nankai accretionary prism revealed from LWD borehole images and their correlation with seismic profile and core data: Results from NanTroSEIZE Stage 1 expeditions, *Geochem. Geophys. Geosyst.*, *12*, Q0AD15, doi:10.1029/2010GC003365.

Theme: Mechanics, Deformation, and Hydrologic Processes at Subduction Complexes, With Emphasis on the Nankai Trough Seismogenic Zone Experiment (NanTroSEIZE) Drilling Transect

Guest Editors: D. Saffer, H. Tobin, P. Henry, and F. Chester

1. Introduction

[2] Logging-while-drilling (LWD) is a technique to obtain geophysical data from the borehole immediately (generally a few minutes) after drilling. This method uses specially designed tools directly connected to the drilling bit, and can avoid alteration of data due to invasion of drilling fluid into permeable lithologies, and can provide reliable data during nonriser drilling where there is limited control on borehole conditions. The technique is thus extremely useful for recording data in weak (unconsolidated) and/or highly deformed sediments, such as accretionary prisms. Several tools can be combined to obtain a variety of geophysical properties and subsurface conditions of rocks and sediments. Resistivity images around the borehole wall can be used to interpret geological features corresponding to bedding planes, fractures and borehole failure (breakouts and tensile fractures), thus is one of the most important data sets for analyzing structural deformation at the cm to dm scale.

[3] LWD is commonly used to acquire borehole geophysical data in the petroleum industry. LWD has been utilized on several previous scientific drilling expeditions; such as ODP Leg 188 [*O'Brien et al.*, 2001], ODP Leg 196 [*Mikada et al.*, 2002; *McNeill et al.*, 2004; *Ienaga et al.*, 2006], ODP Leg 204 [*Trehu et al.*, 2003] and IODP Expedition 308 [*Flemings et al.*, 2006].

[4] IODP Expedition 314 was the first cruise of the international drilling project, NanTroSEIZE [*Kinoshita et al.*, 2008; *Tobin and Kinoshita*, 2006], using the new D/V *Chikyu* in the Nankai Trough subduction zone area. At the Nankai Trough, the Philippine Sea Plate is being subducted at a rate of 4 to 6.5 cm/year along azimuths of 300 to 315° [*Seno et al.*, 1993; *Miyazaki and Heki*, 2001; *Zang et al.*, 2002] underneath the southwest part of Japan. The sediments on the subducting plate are partly scraped off and accreted to the toe of the overriding plate, forming a typical accretionary wedge underlying the inner trench slope. The frontal imbricate thrust zone of the accretionary wedge is bounded by a major out-of-sequence thrust, the megasplay fault system [*Moore et al.*, 2007]. Landward of the megasplay fault system is the Kumano fore-arc basin where sediments are deposited on deformed layers of older accreted sediments.

[5] Expedition 314 was purely designed to acquire LWD data without core, and data were obtained during drilling at four main sites across the fore arc (Figure 1). Site C0002 (Hole C0002A) is located within the Kumano fore-arc basin and drilled through the fore-arc basin deposits and penetrated underlying deformed sediments of the accretionary prism. Sites C0001 and C0004 are located where the megasplay fault system [*Moore et al.*, 2009, and references therein] branches and approaches the seafloor at the seaward edge of the Kumano basin uplift (outer arc high). Site C0006 drilled through the frontal thrust of the accretionary prism. This paper describes the results of the structural analysis performed on the LWD data from these sites, and compares the results with characteristics of seismic reflection profiles and with structural data of cores obtained by the subsequent Expeditions 315 and 316, that drilled at the same sites. These comparisons clarify the scales of geologic

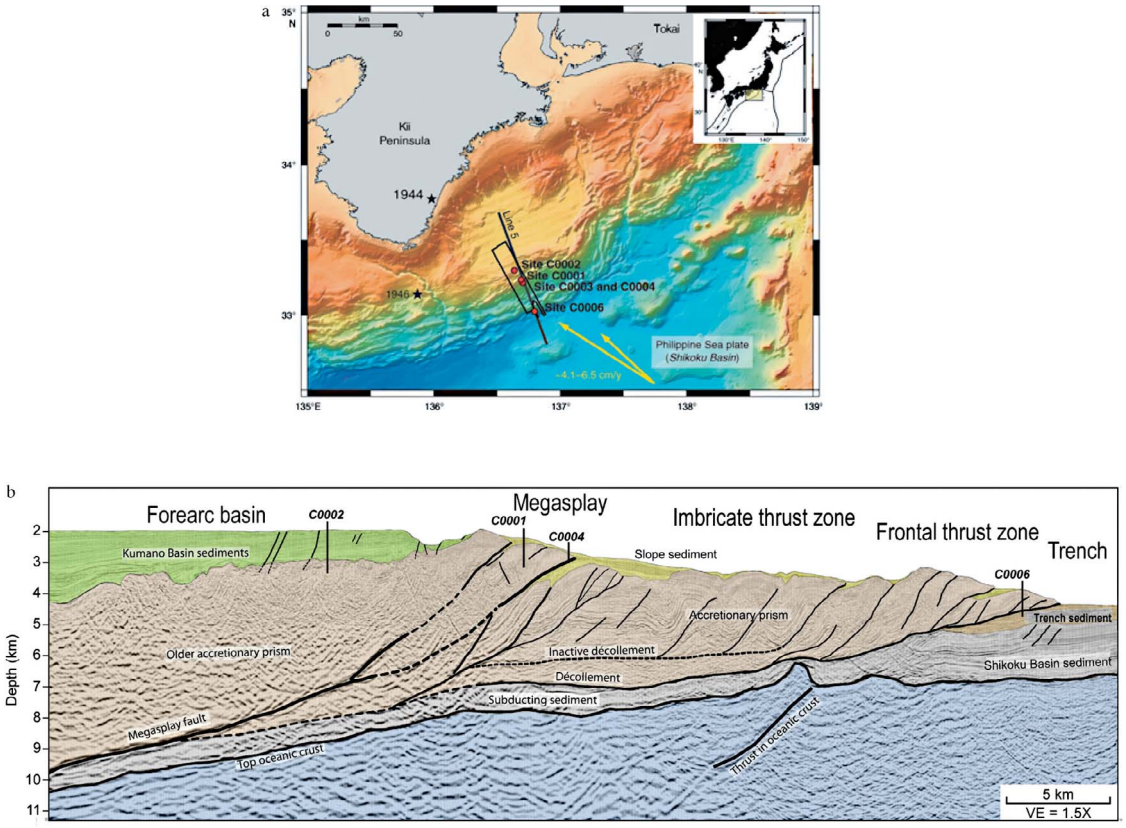

Figure 1. Locations of Sites C0001, C0002, C0004, and C0006 of the NanTroSEIZE Stage I expeditions: (a) map view and (b) section view based on a 2-D seismic reflection profile. Yellow arrows in Figure 1a indicate convergence vectors between the two plates. Stars indicate epicenters of the most recent Nankai plate boundary earthquakes. Section line of Figure 1b is shown in Figure 1a and is subparallel to the longitudinal direction of the rectangular box which represents the 3-D seismic volume area. Plate convergence data from *Seno et al.* [1993] (lower velocity) and *Heki* [2007] (higher velocity).

features that can be obtained by cores, logging and seismic profiles, and the differences in these data sets in terms of methodology and interpreted deformation.

2. Interpretation of LWD Data

2.1. Procedure

[6] We used unwrapped presentations of the 360° borehole resistivity images to interpret structural features (Figure 2). In the GVR (GeoVision Resistivity, trademark of Schlumberger) images, horizontal lines indicate planar surfaces orthogonal to the borehole axis, whereas sinusoidal lines are planar surfaces inclined to the axis. Since natural features (bedding planes, beds, natural fractures and faults) generally have planar geometry at the borehole scale, we used software (Schlumberger Geoframe and GMI Imager) to identify natural features that can be fitted by a sinusoid in the image. The planar features were classified as beds or fractures, and the software automatically calculates and records their depth, dip and azimuth.

[7] Borehole failure, such as "borehole breakouts" and "drilling induced tensile fractures," compression and tension failures due to deformation of the borehole, respectively, were distinguished by their geometry and width. These borehole failure features provide information on the in situ stress orientation and rock strength that can be used to estimate the stress magnitude [e.g., *Zoback*, 2007; *Chang et al.*, 2010; *Moore et al.*, 2011].

[8] Identification of bedding planes needed special care to avoid misinterpretation of several kinds of artifacts [*Expedition 314 Scientists*, 2009]. In order

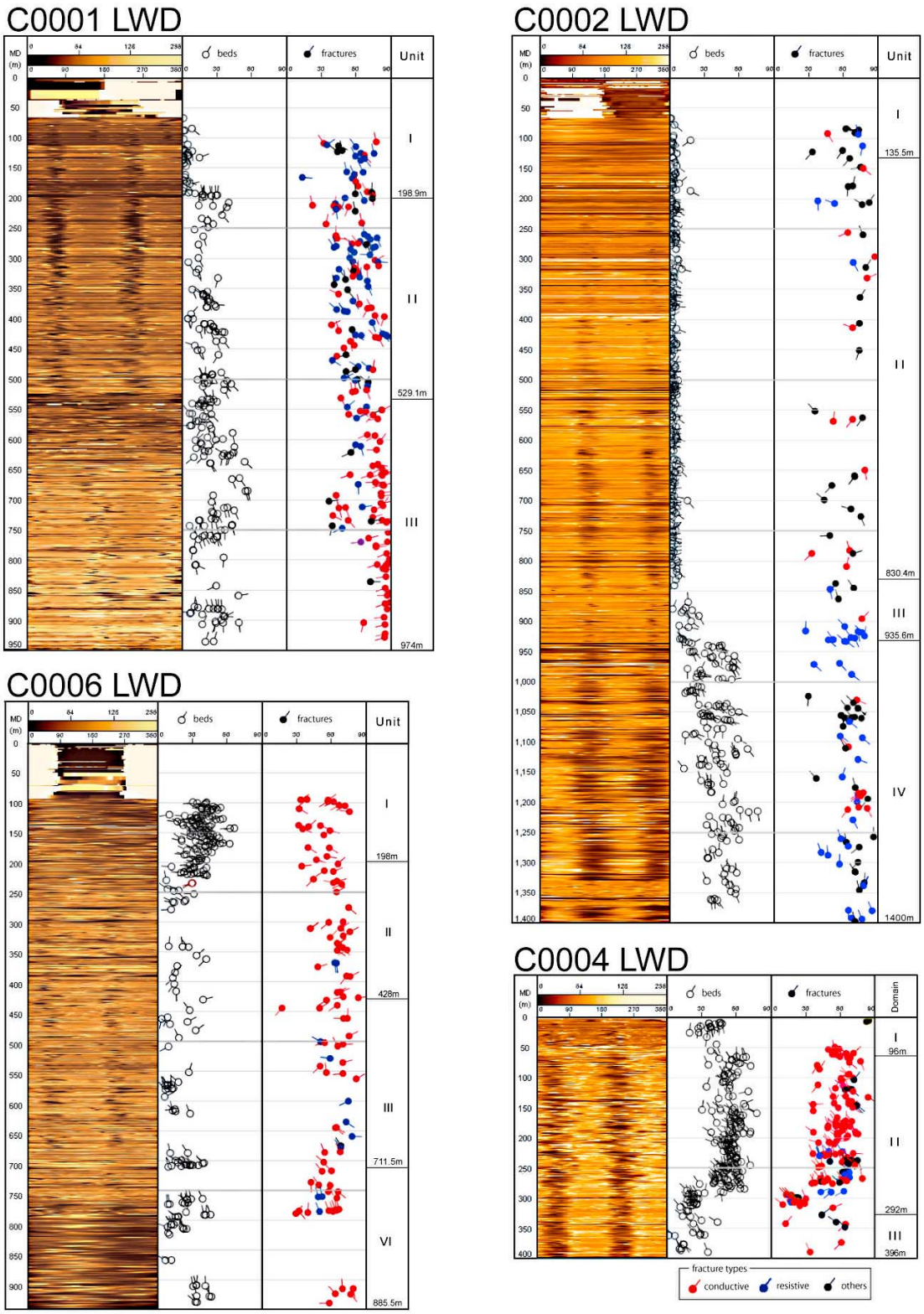

Figure 2. Shallow resistivity images (dynamic normalization, left plot for each site), measured orientations and dips of bedding planes (black, middle plot for each site), and fractures (right plot for each site) of Sites C0001 (Hole D), C0002 (Hole A), C0004 (Hole B), and C0006 (Hole B). Tadpole lines represent dip direction of the plane. Units (C0001, C0002, and C0006) and structural domains (C0004) and their boundary depths are defined by *Expedition 314 Scientists* [2009] based on LWD logging characteristics.

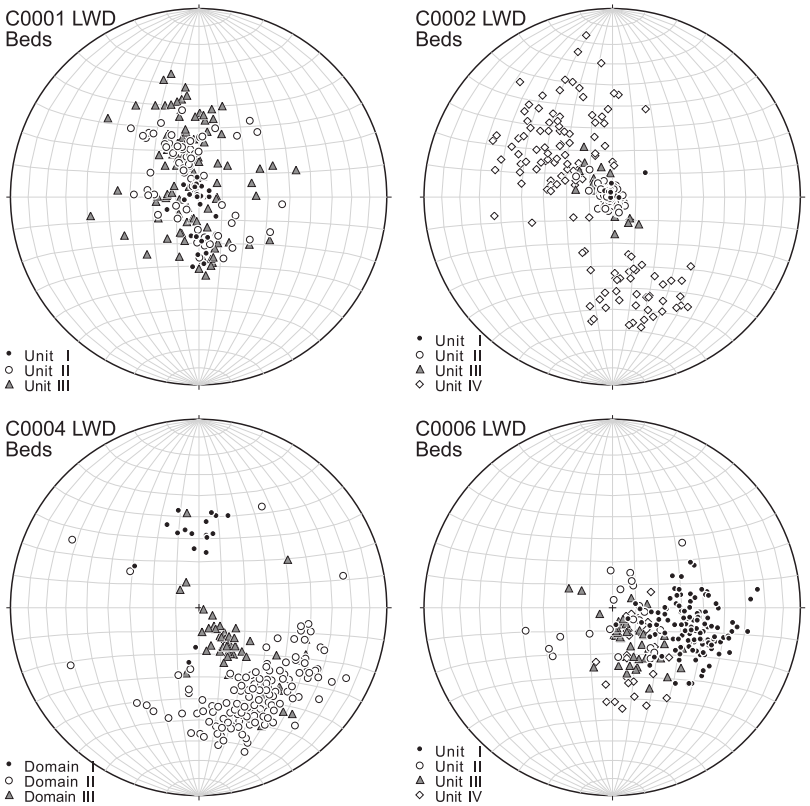

Figure 3. Equal-area lower hemisphere stereographic projection of poles to bedding planes identified in the LWD borehole images. The symbols correspond to the units or domains, defined by *Expedition 314 Scientists* [2009].

to overcome this problem, we compared a variety of images at three different depths of investigation (1, 3, and 5 inch from the borehole wall) using both static and dynamically normalized images (see *Moore et al.* [2011] for further details). We also utilized logging data curves such as "bit resistivity" for overall resistivity responses around the borehole, "ring resistivity" for high-resolution resistivity trend at the bit and "gamma ray" for identification of lithology. The quality of image data is excellent, allowing clear interpretation of planar features. Our interpretations, primarily based on the shallow investigation (1 inch deep from the borehole wall) dynamic images, should have a high degree of accuracy and reproducibility; however, the images favor detection of inclined features relative to sub-horizontal features. Shallowly dipping geological features can be confused with horizontal artifacts due to sharp horizontal changes in gain either during acquisition or dynamic normalization of the data. Details of the image interpretation methodology are given by *Mikada et al.* [2002], *Ienaga et al.* [2006], and *Expedition 314 Scientists* [2009].

[9] Fractures were identified by their anomalous resistivity or conductivity and contrasting dip relative to background sediment and bedding properties in the resistivity images [*Expedition 314 Scientists*, 2009]. Fractures are classified into 3 types: conductive; resistive; and other fractures. "Other fractures" consist of uncertain fractures and fractures of which strike and dip cannot be accurately determined, and those of undefined conductivity are due to small fracture aperture or little/variable resistivity contrast with surrounding sediments.

[10] Our interpretation of the borehole resistivity images includes several types of errors and biases produced by the characteristics of the logging tool and the data. First, since the logging tool measures the electric resistivity around the borehole, only geological features with variations of resistivity can be detected and visualized. Most fractures we identified are conductive but this may be partially due to the visibility of conductive sinusoids against the background of more resistive sediments. Within the very conductive parts of the major fractured zones at C0004B, for example, individual fractures

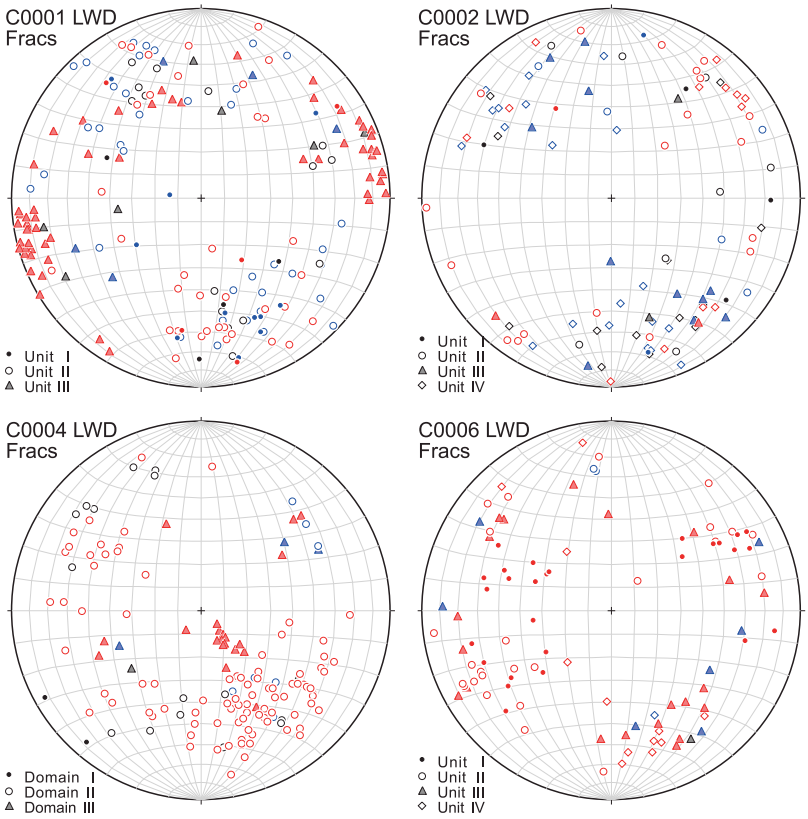

Figure 4. Stereographic projection of poles to fracture planes identified in the LWD borehole images. Note that the two fractures identified in Domain I at Site C0004 may be drilling-induced tensile fractures. All others are natural fractures. The projection method and the symbols are the same as those of Figure 3. The red, blue, and black symbols correspond to open, resistive, and other fracture types, respectively.

are difficult to distinguish and their interpreted dip and azimuth include a certain degree of error. Resistive fractures are only visible where the fracture planes are extremely resistive (e.g., logging Unit IV of C0002A), likely due to mineralization or cementation [e.g., *McNeill et al.*, 2004; *Ienaga et al.*, 2006].

[11] The dip data calculated from the shape of the sinusoids include several types of errors, such as that produced by the data sampling rate (pixel size and hence resolution), borehole conditions and lithology. The pixel size of the LWD borehole image is ~2.5 cm horizontally and 5.0–7.5 cm vertically, and this produces errors in the dip data of approximately 10–15° in the shallow investigation images and 6–9° in the deep investigation images where the planar surfaces are suborthogonal to the borehole axis. More inclined surfaces are less affected by this pixel size/resolution problem, because they can be identified from a larger number of pixels in the image. The borehole conditions and lithology generate errors due to the deviation of the electric current from the originally designed depth of investigation.

2.2. Results of LWD Interpretation

2.2.1. Site C0001 (Megasplay Fault Hanging Wall)

[12] In the borehole images, we identified a number of bedding planes and fractures, and classified the logged interval into three units, based on the characteristics of the structural features. These correspond well with the logging Units defined by *Expedition 314 Scientists* [2009] based on physical properties and lithology from all log data; Unit I (slope basin deposits: 0–198.9 m LSF; LWD depth below seafloor), Unit II (accretionary prism: 198.9–529.1 m LSF) and Unit III (accretionary prism: 529.1–974 m LSF).

[13] In Unit I, bedding dips are mostly gentle (<10°) within the upper 190 m LSF (the majority of

Unit I), then change to higher values (20–30°) dipping to the north (190.5–198.9 m LSF) in the base of the Unit (Figure 3). Bedding dips are steeper in Unit II and include values up to 40°, but show a cluster on the stereonet plot 10–30° dipping to the southeast (Figure 4). In Units III, bedding dips are highly scattered and include values up to 60°. Bedding dips are more difficult to identify in the deeper parts of the hole (particularly between 800 and 880 m LSF) because of the low resistivity contrast in the images.

[14] Fractures identified in the borehole images are both conductive (red tadpoles) and resistive (blue tadpoles; Figure 2). Unit I fractures are both conductive and resistive (Figure 2), and show highly scatter in trend but with dominant trends of NE-SW dip to the north (Figure 4). In Unit II, fractures are again both conductive and resistive, but their dominant trends are NW-SE and steeply (70–90°) dip to both directions. Most fractures in Unit III are conductive (Figure 2) and show a dominant trend of NW-SE, dipping in both directions (Figure 4).

2.2.2. Site C0002 (Kumano Fore-Arc Basin)

[15] *Expedition 314 Scientists* [2009] divided the logged interval into four units; Unit I (0–135.5 m LSF), Unit II (135.5–830.4 m LSF), Unit III (830.4–935.6 m LSF), and Unit IV (935.6–1400 m), using lithological and physical properties characteristics of the logging data.

[16] Bedding dips of Units I–III (fore-arc basin deposits) are mostly shallow (≤15°) (Figure 3). Such shallow dips may be affected by errors due to pixel size in the borehole images, as discussed earlier, and make identifying and accurately determining dip and strike difficult. The poles to the bedding planes are, however, highly concentrated with a NW-SE direction (bedding trends of NE-SW), suggesting sufficient reliability.

[17] The beds of the underlying Unit IV (accretionary prism: 935.6–1400 m LSF) show a NE-SW trend (Figure 3), and are more deformed with steeper dips (range of ~18–60°). The poles to bedding of this unit show two clusters on the stereonet plot (Figure 3): one highly scattered cluster dipping to the south approximately corresponding to the shallow beds (<~1120 m LSF), and the other less scattered cluster dipping to the north corresponding to the deeper beds (>~1120 m LSF).

[18] Fractures were less common at this fore-arc basin site compared with the three sites located within the prism [*Expedition 314 Scientists*, 2009]. Fractures are mostly conductive in Units I and II, resistive in Unit III, and also resistive but with a greater range of conductivity in Unit IV (Figure 4). Fractures of the Units I–III are highly scattered (Figure 4), however, trends of NE-SW to E-W may be present. A few of the Units I–III fractures, with orientations NE-SW and ENE-WSW, show normal offset of bedding planes. Higher fracture densities occur in the upper 200 m and within Unit III (830.4–935.6 m LSF) (Figure 4).

[19] Fractures in Unit IV show much less scatter than in the shallower Unit I–III sediments, and a dominant NE-SW trend with a minor NW-SE trend (Figure 4). Fracture dips are not significantly steeper (~30–85°) than those in Units I–III. Many of the fractures are bedding parallel but their high resistivity allows differentiation from bedding. Several large aperture (10–30 cm) highly resistive fractures were also observed within Unit IV, and these may be cemented or mineralized fractures.

2.2.3. Site C0004 (Megasplay Fault)

[20] Three structural domains were defined based on the pattern of fractures and borehole breakouts in the images [*Expedition 314 Scientists*, 2009]. These domains are slightly different from the Units defined by integrated log characteristics at this site [*Kinoshita et al.*, 2008; *Expedition 314 Scientists*, 2009].

[21] The poles to the bedding plotted in stereographic projection are generally scattered but they also show consistent clusters (Figure 3). Bedding planes in Domain I (slope basin deposits: 0–96 m LSF) are consistent and mostly strike NE-SW and dip 30–40° to the south. The beds in Domain II (accretionary prism: 96–292 m LSF) are more scattered both in dip and azimuth, but generally trend NE-SW and dip 20–70° to the north. Domain III (younger footwall sediments of the megasplay: 292–396 m LSF) shows a less scattered distribution of poles to bedding planes (Figure 3). The dominant bedding plane azimuth and dip direction in Domain III is similar to Domain II (NE-SW) but the dips are generally shallower (average ~20°; range = 5–55°).

[22] Fractures in borehole images are mostly conductive (Figure 2). Domain I shows no measured fracture with the exception of several drilling-induced tensile fractures in the uppermost part of the imaged borehole (depth 56–61 m LSF) [*Expedition*

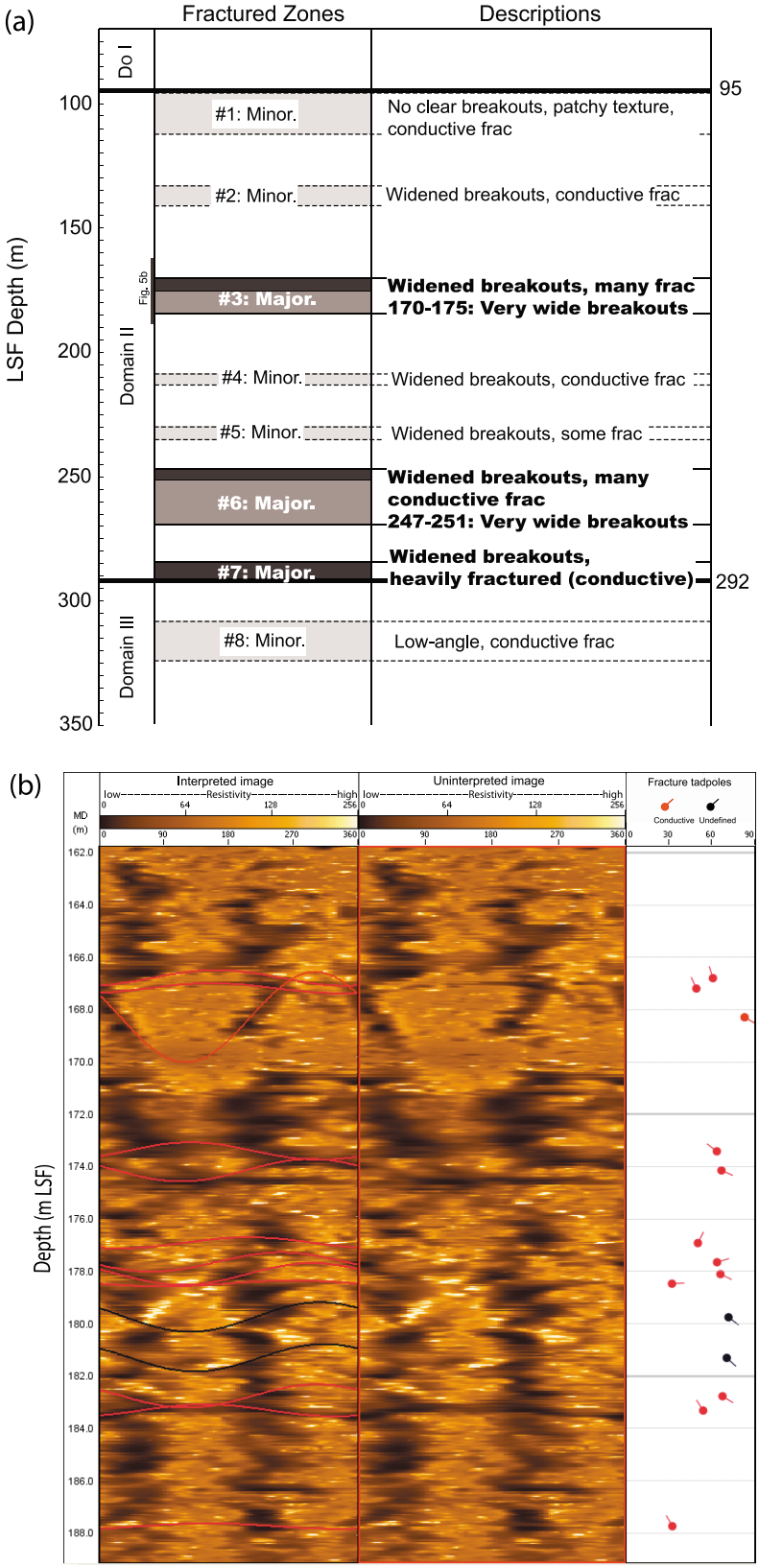

Figure 5. (a) Eight fractured zones defined at Site C0004 based on fracture intensity and borehole conditions. Frac, fractures. (b) The LWD borehole resistivity image shows an intensive fracture development at #3 major Fractured Zone.

314 Scientists, 2009; *Chang et al.*, 2010]. Fractures in Domain II are scattered both in azimuth and dip, but with a dominant trend of NE-SW and mostly steeply dipping (30–70°) to the north (Figure 4). Domain III contains fewer fractures than Domain II (Figure 2) and the poles to the fracture planes form a dominant cluster corresponding to a NE-SW trend and shallower dip (10–20°) to the north (Figure 4). There are also two minor clusters of NW-SE trend dipping both to the east and west.

[23] Eight fractured zones were defined, primarily within Domain II, by intense development of conductive fractures and wide breakouts (Figure 5), and were classified as "major" or "minor" based on intensity of deformation, conductivity and thickness [*Expedition 314 Scientists*, 2009]. All of the major fractured zones are within Domain II and two of these zones are characterized by merged breakouts of extremely broad width producing uniform high-conductivity zones. Based on our borehole image interpretations, the megasplay fault is not a single fault but consists of two major and one minor fractured zones at the base of Domain II (see discussion later).

2.2.4. Site C0006 (Frontal Thrust)

[24] Resistivity images show that the interval shallower than 198 m LSF has a different bedding dip trend from the deeper part of the borehole (Figure 3). This shallow section, interpreted as unconsolidated sediments of the shallow frontal thrust hanging wall, corresponds to Unit I [*Expedition 314 Scientists*, 2009] and deeper section subdivided into Units II (198–428 m LSF), III (428–711.5 m LSF) and IV (711.5–885.5 m LSF). Units II and III comprise the frontal thrust hanging wall and the boundary between Units III and VI approximates the position of the frontal thrust [*Expedition 314 Scientists*, 2009].

[25] Bedding dips are shallow to moderate throughout the logged section, with most dips less than 45°. Bedding orientations are: predominantly westward dip in Unit I; no meaningful cluster in Unit II, and northwestward dips in Units III and IV (Figure 3).

[26] Most fractures are conductive and fracture dips range from ~30–80° with no clear pattern in dip magnitude variation between logging units. Overall fracture orientation is scattered, however, the fractures show a predominant NW-SE strike in Units I and II and a NE-SW strike in Units III and IV (Figure 4). Although some conductive fractures are identified, we are unable to make a clear correlation with the frontal thrust. There is no intensely fractured zone identified in the borehole images at this site.

3. Seismic Reflection and Core Data

3.1. Three-Dimensional Seismic Data

[27] We used the three-dimensional seismic data described by *Moore et al.* [2009]. The data set covers an ~12 km × 56 km area that extends from the Kumano basin seaward to the frontal thrust in the dip direction (orientated at 150.1°) and extends along strike ~4 km northeast and ~8 km southwest of the NanTroSEIZE drilling transect. The 3-D data set was processed through 3-D prestack depth migration (PSDM). The 3-D PSDM clearly images details of faults and small-scale structures, but velocity resolution deeper than ~4500–5000 m is less accurate, due to the short length of the streamers (4500 m) and the strong feathering [*Moore et al.*, 2009].

[28] Seismic resolution is generally defined in terms of the wavelength of the data [*Sheriff*, 1991]. In our study area, the near-surface sediments show P wave velocity of < 1600–1800 m/s and frequency content of ~60–80 Hz [*Moore et al.*, 2009]. These values slightly change to velocities of ~2400 m/s and frequencies of ~40 Hz, at our maximum drilling depths of ~1400 m. These values yield a theoretical limit of vertical resolution $\lambda/4$ (quarter of wavelength) being 5–7 m for near-surface sediments, and 10–20 m for the deepest sediments drilled [*Moore et al.*, 2009]. This resolution is lower where a fresnel zone of seismic wavelet needs to be considered. The fresnel zone, caused by spherical divergence and attenuation of seismic waves, has a diameter *Rf* being $(D\ \lambda/2)^{1/2}$, where *D* is the depth, and this size determines the minimum size feature that can be resolved horizontally in the seismic data set. *Claerbout* [1985] argue that this resolution *Rf* can be just $\lambda/2$ where the data is ideally processed as migrated sections. Based on this assumption, the finest horizontal resolution of the 3-D seismic data set is theoretically 10–14 m for shallow sediments and 20–40 m for the 1400 m deep sediments in this study. The 3-D data set used in this study has a bin size of 12.5 × 18.75 m, which also limits the actual resolution. *Bacon et al.* [2003] described that a 0.5% error in migration velocity can degrade horizontal resolution by a factor of more than 5, suggesting that the horizontal resolution would be lower.

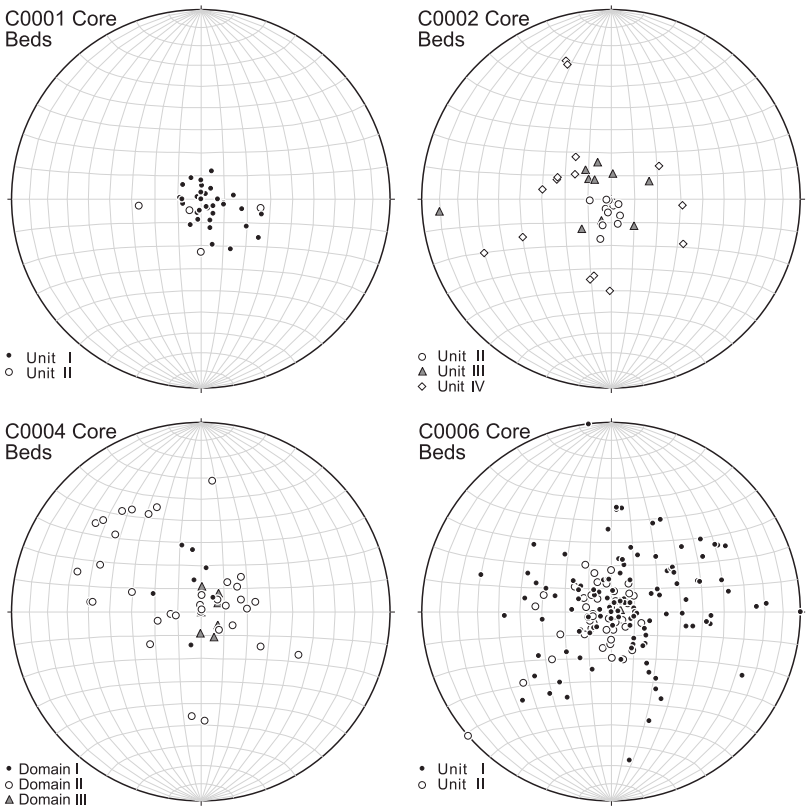

Figure 6. Stereographic projection of poles to bedding planes identified in the cores. The projection method and the symbols are the same as those in Figure 3.

[29] We interpret bedding and fault planes around the four sites in the 3-D seismic data set to compare with the structural features based on LWD and cores. Since the beds and faults are commonly undulating in the 3-D seismic data, we need to make these surfaces flat to calculate dip and azimuth of the planes. A small area of ~20–50 m diameter, corresponding to the finest theoretical resolution of 3-D seismic data of these surfaces (see above) was determined for each structural feature, then a flat surface was calculated by using a least squares fitting method. The orientation of these surfaces was then measured and recorded. Thus the results described in the discussion below are all true dips obtained from the full 3-D volume.

3.2. Core Data

[30] Expedition 315 took core samples from the Sites C0001 and C0002, and Expedition 316 from Site C0004 and C0006 [*Expedition 315 Scientists*, 2009; *Expedition 316 Scientists*, 2009]. D/V *Chikyu* has a CT scanner and all of the cores were scanned to aid in identifying structures and defining their 3-D form and distribution in the core [*Expedition 315 Scientists*, 2009]. Average core recovery at these sites are as follows with drilling depth and % recovery in brackets for each hole: C0001E (0–118 mCSF (core depth below seafloor), 95%), 1F (108–249 mCSF, 98%), 1H (230–458 mCSF, 55%), C0002D (0–204 mCSF, 79%), 2B (475–1057 mCSF, 36%), C0004C (0–135 mCSF, 103%), 4D (100–400 mCSF, 44%) and C0006E (0–409 mCSF, 81%), 6F (395–603 mCSF, 27%).

[31] Orientations of planar features in the cores were determined relative to the core axis and a line representing north in the core reference frame [*Expedition 315 Scientists*, 2009]. Two apparent dips of the planar feature were measured in the core reference frame and converted to a plane represented by a dip and dip azimuth.

[32] Expeditions 315 and 316 routinely used paleomagnetic data to correct drilling-induced rotations of cored sediments. Rotations were induced during Rotary Core Barrel (RCB) coring, and unexpectedly with the Hydraulic Piston Coring System (HPCS). To correct for these rotations, expedition scientists identified sections of cored sediment that were relatively coherent and contin-

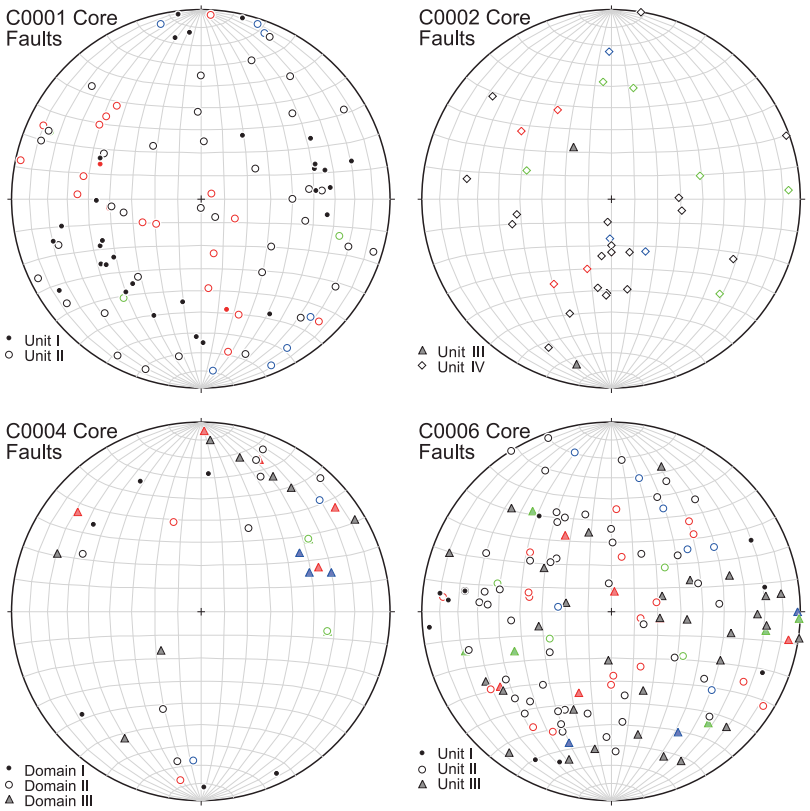

Figure 7. Stereographic projection of poles to fault planes identified in the cores. The projection method and the symbols are the same as those in Figure 3. The black, red, blue, and green symbols correspond to normal, reverse, strike-slip (right-lateral), and strike-slip (left-lateral) faults, respectively.

uous, then matched with paleomagnetic data from the appropriate depth intervals and used these data to unrotate the planar and linear structures preserved in the core section. Individual samples were also measured with the magnetometer on the D/V *Chikyu*, where core samples were fragmented.

[33] We used only those bedding and fault surfaces corrected for rotation using the magnetic measurements in this study, and the poles to bedding (Figure 6) and faults (Figure 7) were stereographically projected in an equal-area lower hemisphere.

4. Structural Style and Comparison of Image Log Data With Seismic Reflection Profiles and Cores

[34] Poles to bedding planes identified in the borehole log images of the four holes show clusters in the NW and SE quadrants of the stereographic projection, especially in the NNW-SSE direction indicating NE-SW trending planes dipping NW and SE (Figure 3). The fracture distributions are more scattered but also show clusters in the NW and SE quadrants (Figure 4). These poles of the bedding planes describe a plane that is approximately parallel to the overall structural trend of the accretionary wedge, and is 60 to 75° oblique to the convergence directions of the Philippine Sea Plate estimated by *Seno et al.* [1993] and *Miyazaki and Heki* [2001] (Figure 1). This suggests that the structural trends, external representation of folds and thrust sheets, may be more strongly controlled by backstop geometry rather than the convergent vector.

[35] In order to determine the structural resolution of the LWD data, we compared these data with the structural data from 3-D seismic interpretation and core descriptions. For comparison with 3-D seismic data, representative bedding planes and fault surfaces identified in the 3-D seismic data set were measured at the four sites (see section 3.1 for methodology) and are presented with borehole image data in Figures 8–10. We also produced 2-D

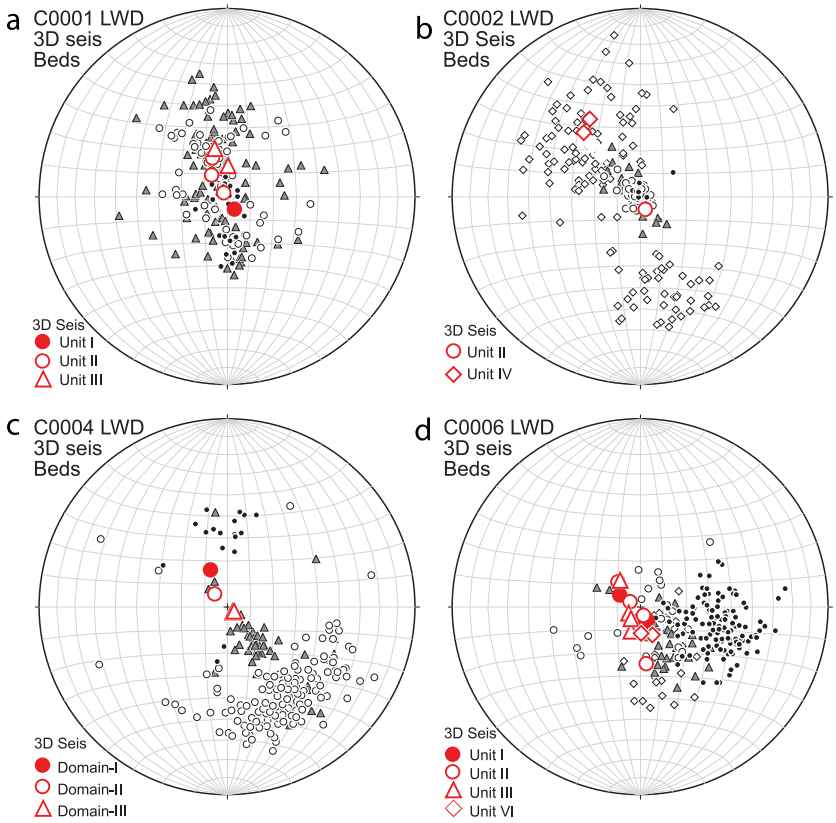

Figure 8. Comparisons of bedding planes identified in the borehole images and those in the 3-D seismic data. The large red symbols in the equal-area lower hemisphere stereographic projection indicate the poles to bedding planes identified in the 3-D seismic data: (a) C0001, (b) C0002, (c) C0004, and (d) C0006. The small black symbols are features identified in the borehole images, using the same symbols as used for each unit/domain for the seismic data results.

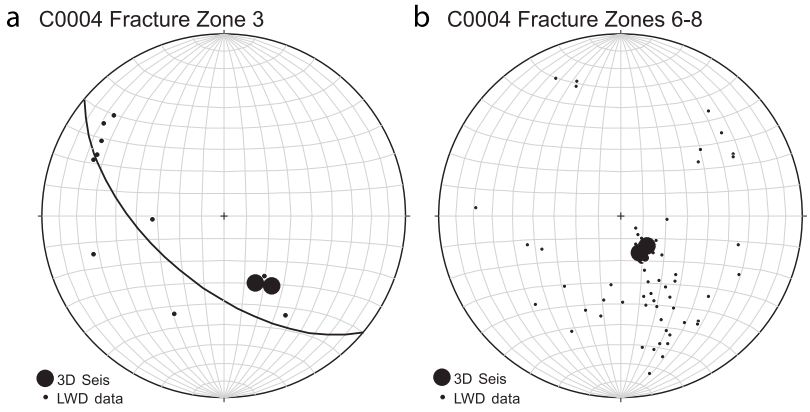

Figure 9. Comparisons of fractures identified in the borehole images and faults in the 3-D seismic data at Site C0004 within discrete fractured zones on an equal-area lower hemisphere stereographic projection. The large symbols indicate the poles to fault planes identified in the 3-D seismic data within (a) Fractured Zone 3 (170–184 m LSF) and (b) Fractured Zones 6–8 (247–324 m LSF), the megasplay fault zone. The great circle in Figure 9a corresponds to the cylindrical fit of the poles to fractures observed in LWD data in Zone 3.

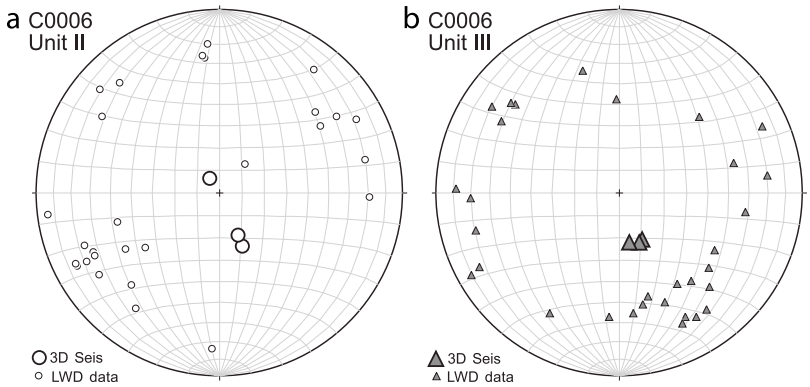

Figure 10. Comparisons of fractures identified in the borehole images and faults in the 3-D seismic data at Site C0006 on an equal-area lower hemisphere stereographic projection. The large symbols indicate the poles to fault planes identified in the 3-D seismic data within (a) Unit II and (b) Unit III.

cross sections in NNW-SSE orientations from 3-D seismic data at each of the four sites, and the apparent dips and fractures from the borehole images are projected along the section lines (Figures 11–14).

4.1. C0001 (Megasplay Fault Hanging Wall)

[36] The individual Units of Site C0001 have distinct structural characteristics (Figures 3 and 4) and

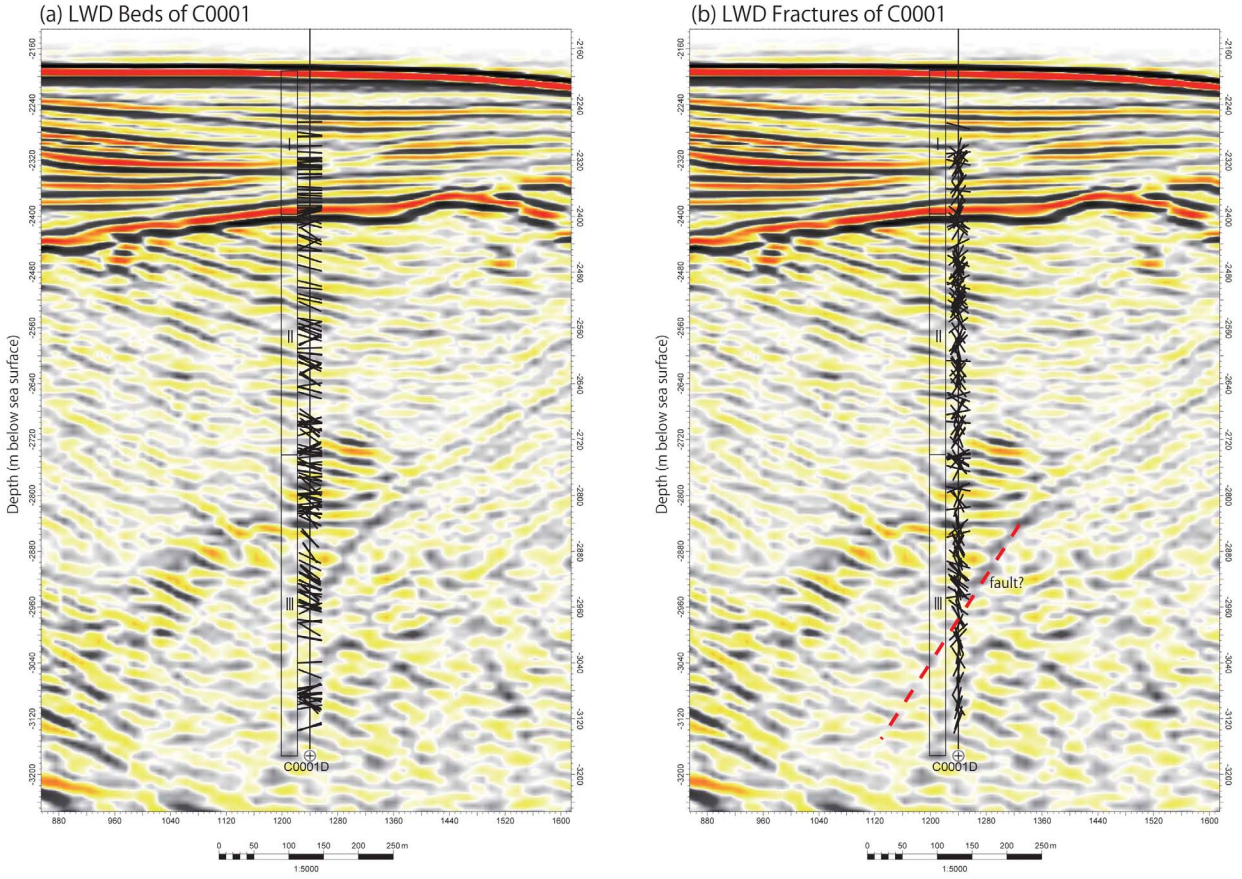

Figure 11. Correlation between seismic profile (from 3-D seismic volume) and structural features identified in the borehole images at Site C0001: (a) beds and (b) fractures. The black bars correspond to apparent dips of these borehole planes in the plane of the profile. The Roman numerals indicate the units defined by *Expedition 314 Scientists* [2009]. A possible fault identified on the profile is also shown in Figure 11b.

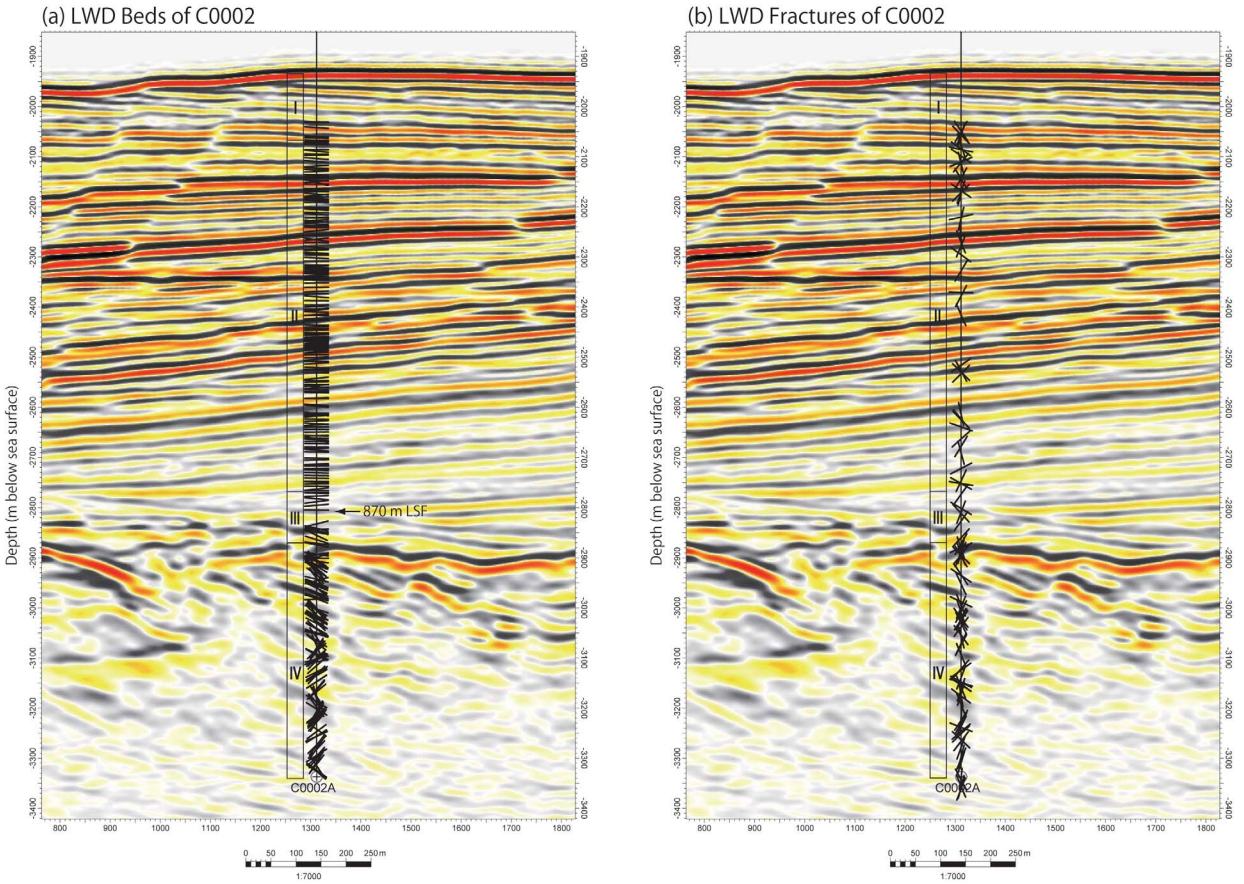

Figure 12. Correlation between seismic profile (from 3-D seismic volume) and structural features identified in the borehole images at Site C0002: (a) beds and (b) fractures. The black bars correspond to apparent dips of these borehole planes in the plane of the profile. The Roman numerals indicate the units defined by *Expedition 314 Scientists* [2009]. The boundary (870 m LSF) of Unit IIIA and IIIB is also shown in Figure 12a.

can be correlated with the 3-D seismic data set and core structures.

[37] Bedding in the 3-D seismic data dips gently within the slope basin deposits just below the seafloor and this interval can be correlated well with the bedding data from resistivity images of Unit I (Figure 11). Core bedding also shows gentle dips, less than 10° (Figure 6). The base of Unit I consists of a long continuous seismic reflection that dips ~5° to the NNW (Figure 8), but the borehole images suggest that beds at this scale dip 20–30° to the north. This difference may be because the thickness of the basal layer (8.4 m) is below the resolution of the reflection data. The cores from this layer also show steepened bedding but details are unresolved because of the disturbances during coring [*Expedition 315 Scientists*, 2009].

[38] In the interval below the slope basin deposits of Unit I (below 198.9 m LSF), the reflection surfaces are of low amplitude and dip ~2–19° to the southeast (Figures 8 and 11). This corresponds well with the beds of Unit II in LWD data that dip (10–30°) to the southeast (Figures 3 and 8). The refection surfaces around 500–700 m below seafloor (LWD Unit III) are subhorizontal and partly in agreement with LWD data (Figure 8) that include gentle dip, although the bedding dips are highly scattered (Figure 8). The position of the disturbed zone (~800–880 m LSF) identified in the borehole image can be correlated with a possible fault dipping to the northwest in the seismic data (Figure 11), however, the fractures identified in the borehole image cannot be directly correlated to the structural features in the seismic data.

[39] The faults identified in the core are highly scattered (Figure 7) and individual faults cannot be correlated to the borehole image structures. *Expedition 315 Scientists* [2009] reported normal

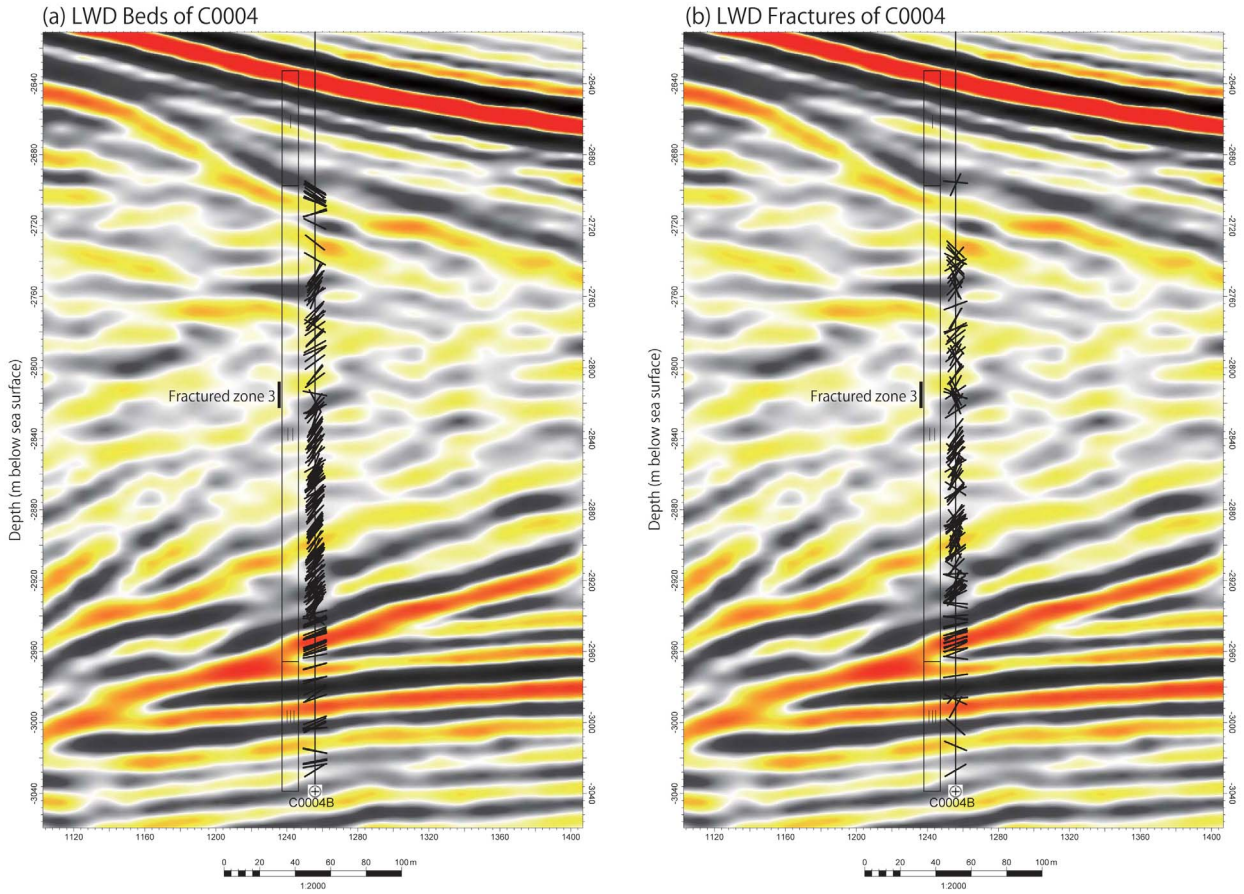

Figure 13. Correlation between seismic profile (from 3-D seismic volume) and structural features identified in the borehole images at Site C0004: (a) beds and (b) fractures. The black bars correspond to apparent dips of these borehole planes in the plane of the profile. The Roman numerals indicate the structural domains defined by *Expedition 314 Scientists* [2009].

faults in the cores trending ~NW-SE while the reverse faults have a NE-SW trend, and these faults are mutually crosscutting. This supports that these faults may have been generated under a stress field of northeast–southwest extension and northwest–southeast shortening. By analogy, the open fractures with a NW-SE direction identified in the borehole images (predominantly developed in Unit III) may have a normal offset, while the fractures trending NE-SW and dipping in both directions (developed in all Units with a variety of fracture types) may be reverse faults (Figure 4). In the cores, shallow dipping strike-slip faults, which cut and postdate normal and reverse faults, may have been reactivated by drilling [*Expedition 315 Scientists*, 2009]. Such a cutting relation by young shallow dipping open fractures can also be observed in borehole images [*Expedition 314 Scientists*, 2009], although with different sense of motion where observed.

4.2. C0002 (Kumano Fore-Arc Basin)

[40] Comparison with seismic data (Figure 12) confirms that Units I–III correspond to the Kumano fore-arc basin deposits and Unit IV is the underlying deformed accretionary prism [*Kinoshita et al.*, 2008]. This was also confirmed from core biostratigraphy [*Expedition 315 Scientists*, 2009].

[41] In the Kumano fore-arc basin, bedding in the seismic data shows gentle dips (>7°) with NE-SW strike and this agrees with bedding orientations from LWD data (Figures 8 and 12). Long continuous reflection bed surfaces in Unit I dip south whereas reflection surfaces in Unit II beds dip gently to the north, e.g., 7° to NNW around 570 m LSF (Figure 8), but the beds identified in LWD data do not show such systematic changes in dip direction between these two units. This may be due to difficulties in resolving low-angle features in resistivity images due to resolution (discussed earlier). The bedding dips in the core are also low

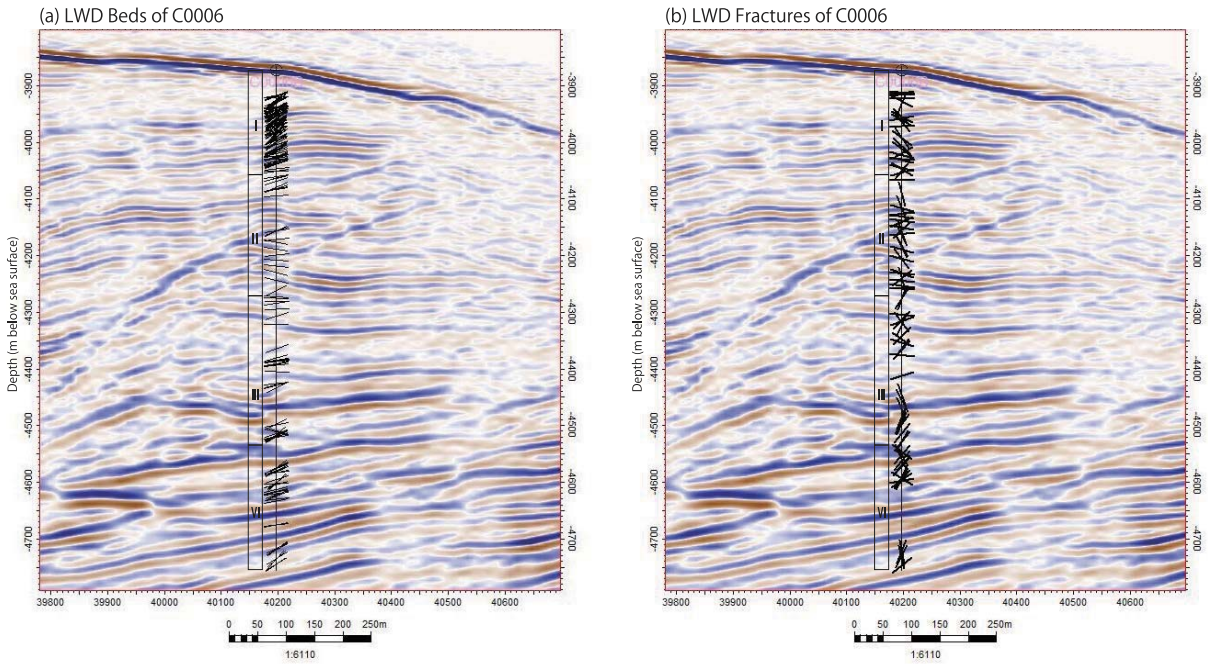

Figure 14. Correlation between seismic profile (from 3-D seismic volume) and structural features identified in the borehole images at Site C0006: (a) beds and (b) fractures. The black bars correspond to apparent dips of these borehole planes in the plane of the profile. The Roman numerals indicate the units defined by *Expedition 314 Scientists* [2009].

angle, less than 10° in Unit I and less than 20° in Unit II.

[42] The basal fore-arc basin sediments (Unit III) can be divided into two subunits in seismic reflection data with a boundary at ~870 m LSF (Figure 12). The lower subunit lacks continuous seismic reflectors and coincides with more intensive fracturing in borehole images (Figure 12). These two subunits have contrasting dip directions in the seismic profile: the upper dipping north and the lower dipping south. LWD bedding interpretations (Figure 3) show NE-SW trends with a consistent dip to the southeast in the lower subunit (Figure 12), which broadly agrees with seismic bedding. The bedding dips of Unit III in cores are scattered but are low angle, less than 20° (Figure 6).

[43] LWD bedding in the accretionary prism strike approximately NE-SW and dip more steeply than those in the Kumano basin (Figure 3). Two clusters of scattered bedding poles suggest the prism must be strongly deformed and likely tightly folded (trending in NE-SW) generating these two dip direction clusters. This agrees with the discontinuous reflectors in the seismic data, which make accurate determination of reflection surface orientation difficult. Overall, the poles to the bedding in Unit IV describe a girdle consistent with a NE-SW trending fold axis. This trend is consistent with the folds in the accretionary prism seaward of Site C0002 in seismic data. Two reflection surfaces measured at ~1060 and 1290 m LSF, plot at the center of one of the two LWD bedding pole clusters (Figure 8), supporting the similarity between the two data sets. The beds in the cores are, however, highly scattered and show no clear trend (Figure 6).

[44] Normal faults are well developed in the fore-arc basin as imaged in seismic reflection data (Figure 12) with trends from E-W to NE-SW and predominantly dipping to the north [*Expedition 314 Scientists*, 2009; *Gulick et al.*, 2010; *Martin et al.*, 2010]. These seismic-scale faults cannot be directly observed in borehole images, but their orientations correlate well with the fore-arc basin fractures in the borehole images (Figure 4), i.e., NE-SW to E-W trends. Most of the faults identified in the

cores show normal slip that have a weak cluster gently dipping to the north (Figure 7), but these individual structures cannot be directly correlated to LWD structures.

[45] Crosscutting relations identified from the core faults suggest that a thrust faulting phase, produced by NW-SE shortening, was followed by two phases of extension in a NE-SW then a N-S direction [*Expedition 315 Scientists*, 2009]. The older thrusts may correspond to the resistive fractures with a NE-SW trend identified in the borehole images in Unit IV accretionary prism sediments (Figure 4). The two orientations of younger extension correspond to the main trends of the borehole fractures, with the NE-SW to N-S directions. The LWD fracture types with a NE-SW trend, in conjunction with core interpretations, may support an interpretation that some thrust faults were reactivated as normal faults in early fore-arc basin history and this reactivation increased complexity of fracture conductivity in the borehole images.

4.3. C0004 (Megasplay Fault)

[46] In Domain I, beds are gently dipping to the SE (Figure 3) and no natural fractures are observed (Figure 4). These characteristics correspond to those of recent slope sediments that deposited subparallel to the seafloor. A reflection surface within this interval dips 19° to SE (Figure 8) around 75 m LSF (Figure 13). Although this is ~10–20° shallower than LWD borehole bed data, the difference is still within error (see earlier discussion). Core beds also show similar trends, ~30° dips to the south to SSE (Figure 6).

[47] In Domain II (the hanging wall thrust sheet of the megasplay), the clusters and trends observed in the poles to LWD borehole bedding and fractures (Figures 3 and 4) suggest that the deformation in this domain is closely related to the regional tectonic environment. The strike of the bedding planes in the borehole images is generally NE-SW and this is approximately parallel to the overall structural trend of the accretionary wedge. The dominant NW dip direction of bedding planes suggests that the folding is asymmetric and has seaward-vergent geometry. This agrees with the typical deformation characteristics of accretionary prisms. Core data are scattered but show a similar structural style, i.e., bedding dipping to the NW or to the SE (Figure 6). From seismic reflection data, clear surfaces dipping to the NW cannot be resolved because of their fragmented nature. One reflection surface measured in Domain II at ~140 m LSF dips 10° to SE (Figure 8), subparallel to the basal reflection of the slope deposits (Figure 13).

[48] Domain III of the LWD data includes gently dipping beds and a few fractures, and correspond to the younger overridden footwall sediments of the megasplay fault in the seismic data, that show continuous and gently (<~30°) dipping reflection surfaces (Figure 13). Two continuous strong reflection surfaces dip ~4° to NW and these are 10–20° shallower than the LWD borehole bed dips (Figure 8). Since the core beds also have gentle dips, less than 10° (Figure 6), this may be due to our bias in interpretation toward steeply inclined features within image log data (as discussed earlier).

[49] The fractured zones identified in LWD borehole data can be correlated directly with the seismic data. The major Fractured Zone 3 (170–184 m LSF, Figure 5b) coincides with the location of a possible landward dipping thrust at this site (Figure 13). The dip and azimuth of this thrust in the seismic data are ~35° and ~330°, respectively (Figure 9a). The poles to this thrust and LWD borehole fracture planes within Fractured Zone 3 roughly form a great circle in stereographic projection assuming a cylindrical fit (Figure 9a). This suggests that the thrust forms a shear zone and its internal fractures show rotation with an axis in a NE-SW direction. Such structural features were not resolved in the cores, because of the poor core recovery around this depth. Poor core recovery is likely a function of the degree of deformation within these zones [*Expedition 316 Scientists*, 2009].

[50] The distinct megasplay fault consists of several strong continuous seismic reflectors in the depth range 252–323 mbsf and coincides with the base of LWD Domain II, and these reflectors dip ~18–21° with a dip direction of 320–335° (Figures 9b and 13). The megasplay fault zone, as imaged in seismic data, corresponds to the major Fractured Zones 6 (247–269 m LSF) and 7 (284–292 m LSF) and minor Fractured Zone 8 (308–324 m LSF) in LWD borehole image data. The poles to the splay fault surfaces from seismic data are positioned near to the center of the LWD borehole fracture pole clusters within Zones 6 to 8 (Figure 9b). These results support the suggestion that the splay fault zone, as imaged seismically, consists of a number of shear fractures subparallel to the main fault zone. This is supported by core observations that reported brecciated rock at this depth, although core recovery is quite poor.

[51] Crosscutting relations of core faults and borehole fractures are not clear at this site. This is partly because of the poor core recovery due to intense deformation around the megasplay fault zone, and also because most LWD fractures have similar trend and no fractures have visible offset, therefore relative timing cannot be determined.

4.4. C0006 (Frontal Thrust)

[52] In Unit I, the bedding in the borehole images dips ~40° toward the west (Figure 3), with core bedding including dips up to 70° but trends quite scattered (Figure 6), however, beds dip gently (~10°) to the SE or NW at the seismic reflection scale (Figure 8). Again, the structural data from seismic reflection are all true 3-D dips. The SE dipping beds in the seismic data are located in the shallowest sediments and are subparallel to the seafloor, thus supporting interpretation as slope sediments. The reflection surfaces dipping NW are relatively continuous and maybe turbiditic sediments (Figure 14). The dip of these surfaces is significantly gentler than the values estimated from borehole images at equivalent depths (Figures 8 and 14). It should be noted that the LWD borehole bedding dips displayed on Figure 14 are "apparent dips" projected onto the NW-SE seismic profile, thus their dip is less than true dip. However, the difference between the true dips of LWD borehole and seismic reflections beds is apparently real and cannot be neglected. *Expedition 314 Scientists* [2009] interpreted these LWD borehole beds as affected by gravitational slumping toward the west, and this process may generate small-scale structural features detected in borehole images but below the resolution of the seismic data. Core observations reported that minor faults trending N-S to NW-SE are normal faults in Unit I [*Expedition 316 Scientists*, 2009] (Figure 7) and this suggests that the LWD open fractures trending N-S to NW-SE may also have normal offset, although no offset was observed in initial investigations (Figure 4). This direction and sense of shear suggest the deformation structures observed in the borehole images may have been generated under an extensional environment, probably due to shallow slope failure.

[53] The beds in Unit II (thrust sheet) are gently dipping to the NW and SE in the 3-D seismic data and this differs from those identified in the borehole images which have a range of trends but includes a cluster dipping shallowly to the NNW (Figure 8). The bedding planes in the cores are highly scattered but Figure 6 shows that Unit II beds show more gentle dips and less scattered distributions than those of Unit I. This feature is similar to that identified in the borehole images (see Figure 3). Unit III and IV beds are gently (>12°) dipping in the seismic data and this is consistent with the borehole image bed data (Figure 8). Coring at Site C0006 did not reach Unit III and IV.

[54] The seismic data show several imbricate thrust faults of ~7–26° dip to the NNW in Unit II and III (Figures 10 and 14) and the biostratigraphy constructed from core samples confirmed several stratigraphic repetitions [*Expedition 316 Scientists*, 2009]. The core samples obtained from 230 to 545 m below seafloor are strongly fractured, and striated or polished planes are common [*Expedition 316 Scientists*, 2009]. This is clearly due to several thrust faults in this interval that can be identified in the seismic data (Figure 10). The LWD borehole images do not show obvious major faults or fractured zones, however zones of more intense fracturing are observed. In some cases, conductive fractures may correlate with seismically inferred thrust faults. In core samples, the seismic faults were identified as strongly fractured or brecciated intervals [*Expedition 316 Scientists*, 2009], suggesting that the faults form broad shear zones consisting of a number of minor faults. Since these minor faults may have small aperture, their minimal resistivity contrast with surrounding sediments may prevent identification in LWD image data. The small aperture of the faults may also be due to relatively soft sediment properties (low Young's Modulus and high Poisson's ratio) and the low intensity of strain at this site compared to C0001 and C0004, located further landward in the accretionary prism.

[55] From seismic data, and from log properties, the frontal thrust is likely located at the boundary between Units III and IV, however no significant fault zone is identified within borehole images. The character of the frontal thrust is markedly different in seismic and image log data at Site 808 along the Muroto transect of the Nankai Trough where a distinct resistive fault zone with conductive fractures is observed in resistivity images [e.g., *McNeill et al.*, 2004; *Ienaga et al.*, 2006]. One explanation may be that strain at the Site C0006 frontal thrust may be lower than at Site 808, where the thickness of incoming sediments is approximately half of that seaward of C0006B [*Expedition 314 Scientists*, 2009]. Coring at Site C0006 did not reach the frontal thrust and any comparisons of faults

between the three data sets are therefore only in the hanging wall.

[56] Crosscutting relations and the relative timing of core faults and LWD fractures are not clear at this site. Neither fault offset nor crosscutting fractures can be identified in the borehole images and faults are, in general, rather poorly developed. No interpretations of crosscutting relationships are provided from initial interpretations of cores at this Site [*Expedition 316 Scientists*, 2009].

5. Similarity and Differences in Structural Styles at Different Scales

[57] There are many general similarities in the structural styles based on our interpretations of LWD borehole images, cores and 3-D seismic data set. A typical example is the slope basin deposits that generally show gentle dips (~20°) to the south to SSE in all three data sets of different scales (e.g., Unit I of C0001, Domain I of C0004). Kumano fore-arc basin deposits (Units I–III of C0002) and the footwall of the megasplay fault (Domain III of C0004) also show gentle (~10°) dips in LWD borehole images, core beds and 3-D seismic, although LWD beds include some dips to 20° that may result from resolution problems of low dipping horizons (see earlier).

[58] In detail, there are differences, beyond resolution-related errors, in the structural styles exhibited in the LWD borehole images and those in the seismic and core data, which may be either real or controlled by what can be coherently imaged. The reduced image coherence and resolution of the seismic data in Units II and III at C0001, Unit IV at C0002 and Domain II at C0004 are likely due to the highly deformed strata of the accretionary wedge where reflection surfaces are fragmented or seismic waves are scattered. Such intensity of deformation is also supported by the highly scattered bedding dips observed in core samples (Figure 6).

[59] Actual differences in structural styles at the different scales can also be observed. For example, Unit I beds of C0006B dip in different directions in borehole images, cores and seismic data. As discussed earlier, this may be produced by small-scale deformation due to slumping of sediments, that cannot be detected by reflection seismology. Another example is the basal layer of Unit I of C0001 that dips 20–30° to the north in LWD and cores, while 3-D seismic data show this layer gently (~5°) dipping to the NNW. The overall geometry of this layer may be gentle as shown in seismic data, but the layer may consist internally of thin beds dipping in 20–30° to the north, that can only be detected by LWD and core data.

[60] One important aspect is the methodology used for acquiring each data set. Reflection seismology uses rock responses of acoustic impedance (sonic velocity and rock density), whereas the LWD borehole images in this study use resistivity responses of borehole wall rocks and sediments. Thus these two data sets are fundamentally based on different physical properties, both also differ from optical observations (e.g., of cores), and may therefore indicate different structural features and styles. Production of seismic profiles requires a velocity model, and this seismic velocity model incorporates errors that may explain some of the differences with borehole trends.

[61] The structural data obtained by core observations tend to be generally more scattered than the other two data sets. This may be produced by disturbances during coring and errors in orientation estimation, or may be real and a function of scale of observation. Acquisition of cores produces shear strain of the rocks at the drilling bit and this may reactivate natural discontinuity surfaces. Such artificial reactivation of natural structures may be extremely difficult to distinguish from natural deformation, and the resultant structural data based on core observation may include errors that cannot be evaluated quantitatively. Core orientations are determined using paleomagnetic measurements [*Expedition 315 Scientists*, 2009; *Expedition 316 Scientists*, 2009], which also introduces errors. This is because the method is based on several assumptions, including horizontal or subhorizontal bedding, no vertical axis rotation, and vertical core [*Expedition 315 Scientists*, 2009]. These cannot be applied to Units where beds are highly deformed and which have also probably experienced vertical axis rotation without introducing potential error.

[62] The bedding dips identified in the seismic data are generally shallow and clustered while those in the borehole images are steeper and more scattered in this study. Scattering of borehole image data may in part be related to the reduced accuracy of fitting a plane sinusoid to low dipping planes. For 3-D data, the reliability of surface orientations generally depends on the width of the 3-D seismic cube and this must also be considered. At C0006B,

the width of the seismic cube is narrower than at other sites and the reliability may be reduced.

[63] Our interpretations suggest that seismic-scale faults are not always identified clearly in the borehole images. Typical examples include the normal faults in the Kumano basin deposits at C0002 and the thrust faults in Unit II–III (frontal thrust hanging wall and frontal thrust) at C0006. The basin normal faults are interpreted from offset of seismic reflectors, while the thrusts at C0006 show fault plane reflections with possible reflector displacement. In the seismic profiles, these faults show displacement of at least a few meters, thus they may have a width of a few centimeters or more, and may be significantly larger than the pixel size of the borehole images. In addition, the fault resistivity contrast with surrounding rocks may be minimal at these sites. Both factors may reduce the likelihood of imaging a discrete fault plane in the borehole resistivity image data.

[64] The megasplay fault and the landward dipping thrust within the megasplay hanging wall at C0004 are also seismically clear but they are not so obvious in the borehole images. Instead, the megasplay fault is recognized as a series of discrete fractures in borehole images. As discussed earlier, orientation of each fracture within these zones is not always parallel to the general orientation of these major thrusts, but may correspond to internal rotation within the shear zones. This suggests that major faults with wide deformation zones are recognized as "fracture-concentrated zones" within borehole images and the overall orientation of the major faults should be determined from seismic reflection data.

[65] LWD borehole data may typically be used for observations of detailed structural styles at finer scales whereas seismic data are used for overall geometry at larger scales. Core samples provide the finest-scale structural styles and are therefore complementary to log and seismic data, but core recovery is generally incomplete particularly in deformed intervals. Best practice for combining these data sets, therefore, requires a deep understanding of the nature of the data and the theoretical background of each technique, and of the likely variation in deformation style at different scales highlighted by this study.

6. Conclusions

[66] The structural features identified in the LWD borehole resistivity images show that the strata drilled at four sites across the Nankai Accretionary Prism can be correlated to the geological characteristics of reflection surfaces on seismic profiles and, in some cases, with structures in cores. Correlation between LWD and seismic data is generally better for bedding dips than for small-scale fractures. Seismic-scale faults are not always detected clearly in borehole images, particularly if the fault has minor resistivity contrast with surrounding rocks. However, the internal fracture patterns of the fault zone can often be identified from borehole log images. Several cross sections of the drilling intervals show contrasting structural styles between the borehole images and the seismic data and this may be produced by the different scale of observations (cm scale in the borehole images and scale of tens of meters in the seismic data) and hence a result of real differences in deformation at different scales and/or by limits of resolution and errors. LWD can be a powerful tool to bridge the data gap between core and seismic scales and highlights how deformation style changes across different scales. Care should be taken, however, in comparison between data sets from cores, geophysical logging and seismic profiles, to understand the characteristics of these data and the theoretical background of the methodologies and their respective resolutions, errors and uncertainties.

Acknowledgments

[67] This research used data provided by the Integrated Ocean Drilling Program (IODP). Funding for this research was provided by a Grant-in-Aid for Scientific Research (KAKENHI: 213101115) and by a Grant-in-Aid for Scientific Research on Innovative Areas (21107002). The authors acknowledge Center for Deep Earth Exploration (CDEX), Japanese IO, who supported the onboard scientists during the expedition. Y.Y. and Y.N. also acknowledge Japan Drilling Earth Science Consortium (J-DESC) for its generous support. We acknowledge the structural teams of IODP NanTroSEIZE Stage 1 Expeditions 315 and 316. The seismic team members of Expedition 314 are highly acknowledged for their constructive comments and cooperation to produce Figures 11–13 during the expedition. Reona Masui also helped production of Figure 14. This paper was greatly improved by comments by two reviewers, Gaku Kimura and Sean Gulick.

References

Bacon, M., R. Simm, and T. Redshaw (2003), *3-D Seismic Interpretation*, Cambridge Univ. Press, Cambridge, U. K.

Chang, C., L. C. McNeill, J. C. Moore, W. Lin, M. Conin, and Y. Yamada (2010), In situ stress state in the Nankai accretionary wedge estimated from borehole wall failures, *Geochem. Geophys. Geosyst.*, *11*, Q0AD04, doi:10.1029/2010GC003261.

Claerbout, J. (1985), *Imaging the Earth's Interior*, Blackwell Sci., Palo Alto, Calif.

Expedition 314 Scientists (2009), Expedition 314 report, *Proc. Integrated Ocean Drill. Program*, *314/315/316*, doi:10.2204/iodp.proc314315316.111-118.2009.

Expedition 315 Scientists (2009), Expedition 315 report, *Proc. Integrated Ocean Drill. Program*, *314/315/316*, doi:10.2204/iodp.proc314315316.121-124.2009.

Expedition 316 Scientists (2009), Expedition 316 report, *Proc. Integrated Ocean Drill. Program*, *314/315/316*, doi:10.2204/iodp.proc314315316.131-136.2009.

Flemings, P. B., J. H. Behrmann, C. M. John, and Expedition 308 Scientists (2006), *Proceedings of the Integrated Ocean Drilling Program*, vol. 308, Integrated Ocean Drill. Program, College Station, Tex., doi:10.2204/iodp.proc.308.2006.

Gulick, S. P. S., N. L. Bangs, G. F. Moore, J. Ashi, K. M. Martin, D. S. Sawyer, H. J. Tobin, S. Kuramoto, and A. Taira (2010), Rapid forearc basin uplift and megasplay fault development from 3D seismic images of Nankai margin off Kii Peninsula, Japan, *Earth Planet. Sci. Lett.*, *300*, 55–62, doi:10.1016/j.epsl.2010.09.034.

Heki, K. (2007), Secular, transient and seasonal crustal movements in Japan from a dense GPS array: Implication for plate dynamics in convergent boundaries, in *The Seismogenic Zone of Subduction Thrust Faults*, edited by T. Dixon and C. Moore, pp. 512–539, Columbia Univ. Press, New York.

Ienaga, M., L. C. McNeill, H. Mikada, S. Saito, D. Goldberg, and J. C. Moore (2006), Borehole image analysis of the Nankai Accretionary Wedge, ODP Leg 196: Structural and stress studies, *Tectonophysics*, *426*, 207–220, doi:10.1016/j.tecto.2006.02.018.

Kinoshita, M., H. Tobin, M.K. Thu, P. Gaillot, and Expedition 314 Scientists (2008), NanTroSEIZE stage IA: NanTroSEIZE LWD transect, *Integrated Ocean Drill. Program Prelim. Rep.*, *314*, 1–63.

Martin, K. M., S. P. S. Gulick, N. L. B. Bangs, G. F. Moore, J. Ashi, J.-O. Park, S. Kuramoto, and A. Taira (2010), Possible strain partitioning structure between the Kumano fore-arc basin and the slope of the Nankai Trough accretionary prism, *Geochem. Geophys. Geosyst.*, *11*, Q0AD02, doi:10.1029/2009GC002668.

McNeill, L. C., M. Ienaga, H. Tobin, S. Saito, D. Goldberg, J. C. Moore, and H. Mikada (2004), Deformation and in situ stress in the Nankai Accretionary Prism from resistivity-at-bit images, ODP Leg 196, *Geophys. Res. Lett.*, *31*, L02602, doi:10.1029/2003GL018799.

Mikada, H., et al. (2002), *Proceedings of the Ocean Drilling Program, Initial Reports* [CD-ROM], vol. 196, Ocean Drill. Program, College Station, Tex.

Miyazaki, S., and K. Heki (2001), Crustal velocity field of southwest Japan: Subduction and arc-arc collision, *J. Geophys. Res.*, *106*, 4305–4326, doi:10.1029/2000JB900312.

Moore, G. F., et al. (2007), Three-dimensional splay fault geometry and implications for tsunami generation, *Science*, *318*, 1128–1131, doi:10.1126/science.1147195.

Moore, G. F., et al. (2009), Three-dimensional splay fault geometry and implications for tsunami generation, *Proc. Integrated Ocean Drill. Program*, *314/315/316*, doi.10.2204/iodp.proc314315316.102.2009.

Moore, J. C., C. Chang, L. McNeill, M. K. Thu, Y. Yamada, and G. Huftile (2011), Growth of borehole breakouts with time after drilling: Implications for state of stress, NanTroSEIZE transect, SW Japan, *Geochem. Geophys. Geosyst.*, *12*, Q04D09, doi:10.1029/2010GC003417.

O'Brien, P. E., et al. (2001), *Proceedings of ODP Initial Reports* [CD-ROM], vol. 188, Ocean Drill. Program, College Station, Tex.

Seno, T., S. Stein, and A. E. Gripp (1993), A model for the motion of the Philippine Sea plate consistent with NUVEL-1 and geological data, *J. Geophys. Res.*, *98*, 17,941–17,948, doi:10.1029/93JB00782.

Sheriff, R. E. (1991), *Encyclopedic Dictionary of Exploration Geophysics*, 3rd ed., Soc. of Explor. Geophys., Tulsa, Okla.

Tobin, H. J., and M. Kinoshita (2006), NanTroSEIZE: The IODP Nankai Trough Seismogenic Zone Experiment, *Sci. Drill.*, *2*, 23–27, doi:10.2204/iodp.sd.2.06.2006.

Trehu, A. M., et al. (2003), *Proceedings of ODP Initial Reports* [CD-ROM], vol. 204, Ocean Drill. Program, College Station, Tex.

Zang, S. X., Q. Y. Chen, J. Y. Ning, Z. K. Shen, and Y. G. Liu (2002), Motion of the Philippine Sea plate consistent with the NUVEL-1A model, *Geophys. J. Int.*, *150*(3), 809–819, doi:10.1046/j.1365-246X.2002.01744.x.

Zoback, M. D. (2007), *Reservoir Geomechanics: Earth Stress and Rock Mechanics Applied to Exploration, Production and Wellbore Stability*, 449 pp., Cambridge Univ. Press, New York, doi:10.1017/CBO9780511586477.